buildings

Article

Study on the Impact Dynamics and Fracture Morphology of Cement-Improved Aeolian Sand Under Freeze–Thaw Cycles

Xunchang Li [1,2], Kexin Ren [1,2,*], Yuang Qi [1] and Xuqing Pang [3]

1 School of Geological Engineering and Geomatics, Chang'an University, Xi'an 710061, China
2 Key Laboratory of Western China's Mineral Resources and Geological Engineering, Ministry of Education, Xi'an 710054, China
3 Shaanxi Railway Institute, Weinan 714099, China
* Correspondence: 2024126135@chd.edu.cn

Abstract

Cement-improved aeolian sand is a potentially sustainable geomaterial that has been used in engineering applications such as subgrade filling and slope stabilization in cold regions. To investigate the degradation patterns of the dynamic mechanical properties of improved aeolian sand following freeze–thaw cycles, this study conducted the Split Hopkinson Pressure Bar (SHPB) test on cement-improved aeolian sand under different freeze–thaw cycle numbers and cement content, revealing its dynamic mechanical characteristics, energy dissipation patterns, and failure mechanisms. The results indicate that, as the number of freeze–thaw cycles increased, internal microcracks progressively develop and propagate, and the dynamic mechanical properties of the modified soil gradually deteriorate. This is manifested by a gradual decrease in the dynamic peak stress, a decline in the dissipated energy density, and an upward trend in the fractal dimension of the fragment mass. Compared to the deterioration observed during the first ten freeze–thaw cycles, the magnitude of the changes in dynamic mechanical parameters decreased, indicating a gradual reduction in the overall rate of deterioration. The addition of cement enhances the frost resistance of the modified soil; however, an excessively high cement content shifted the failure mode toward brittle fracture. and the fractal dimension exhibits a decreasing trend. The conclusions of this study offer a theoretical framework for catastrophe mitigation in cement-improved aeolian sand, including freeze–thaw and dynamic loading.

Keywords: cement-improved aeolian sand; impact mechanical properties; freeze–thaw cycles; damage mechanisms; SHPB

Academic Editor: Salvatore Verre

Received: 31 July 2026
Revised: 10 September 2026
Accepted: 11 September 2026
Published: 15 September 2026

1. Introduction

Aeolian sand is a sandy soil formed when wind transports sand and gravel particles to alluvial plains. Aeolian sand can serve as an economical fill material in arid regions where conventional construction materials are scarce or costly to transport [1]. However, the direct engineering use of aeolian sand is limited by its low cohesion, high permeability, and low shear strength [2]. For the resource exploitation of aeolian sand, a number of academics have suggested physical and chemical enhancement methods [3]. Physical improvements include mechanical compaction and the addition of geosynthetic materials [4], but these methods face limitations such as limited durability and strength enhancement. Chemical modification involves incorporating chemical materials to improve performance, creating strong bonds between aeolian sand particles to enhance strength and improve cohesion.

Common modification materials include cement, clay powder, and fly ash [5]. Among these, the cement modification method is the most widely used, applied in road embankments, dam construction, and building reinforcement projects, providing important practical experience and theoretical support for the resource utilization of aeolian sand.

In China's northwestern regions, infrastructure is frequently susceptible to freeze–thaw cycles. These cycles weaken material strength, promote fracture propagation, and can even result in structural failure, jeopardizing facility safety [6]. As a result, studying the mechanical properties of innovative modified soils during freeze–thaw cycles has been a primary focus. Baldovino et al. [7] studied how freeze–thaw cycles and the cement content affected the mechanical characteristics and durability of cement-modified silt. The findings revealed that the frequency of freeze–thaw cycles had a negative impact on the specimens' splitting tensile strength and unconfined compressive strength, and that this deterioration in mechanical parameters was directly connected to microporosity. Based on triaxial compression tests, Cui [8] analyzed the synergistic effects of temperature and the sand–cement ratio on the static mechanical properties of modified aeolian sand, determining the optimal sand–cement ratio for enhancing the static mechanical properties under elevated temperature conditions. Meanwhile, Chen Rui [9] found that cement significantly improves the mechanical properties of hardened aeolian sand under freeze–thaw cycles, such as the shear strength and internal friction angle. He also explained the strengthening mechanism of cement from a microscopic perspective [10]. Ruan Bo [11] utilized dynamic triaxial tests to investigate the dynamic mechanical properties of fiber-cement-modified aeolian sand, concluding that the dynamic elastic modulus of the modified aeolian sand specimens decreases exponentially with the number of freeze–thaw cycles. He also established a service life prediction model for fiber-cement-modified aeolian sand under freeze–thaw conditions, providing a basis for evaluating the stability of cement-improved aeolian sand [12]. The existing research has primarily focused on the static properties and fatigue behavior of cement-improved aeolian sand under small strains. However, in actual engineering applications, the material may also be subjected to impact loads caused by blasting operations, the operation of heavy machinery, vehicle impacts, and seismic activity, all of which affect the stability and service life of the infrastructure [13]. Under such impact conditions, the failure modes of the material often undergo significant changes.

The SHPB test is commonly used for studying the dynamic behavior and fracture properties of rock and concrete under impact stresses [14]. Zhang [15] investigated the dynamic mechanics of damaged fissured sandstone and used digital image analysis to track the evolution of the material's damage strain field. The researchers discovered that freeze–thaw cycles worsened damage, changing the crack pattern from localized to diffused. Shu et al. [16] analyzed the effect of low temperatures on the impact performance of cement-stabilized soil and, by examining micro-structures, further elucidated the failure mechanisms of concrete under dynamic loading. Additionally, since crack propagation in materials under impact loading is related to energy conversion, some researchers have conducted studies from an energy perspective. Luo [17] analyzed the effects of freeze–thaw cycles on the total strain energy and elastic strain energy of specimens from the perspective of energy evolution, thereby revealing the extent of internal mechanical damage. Zhu et al. [18] developed a constitutive model to explain the stress–strain relationship of frozen soil and used dissipated energy to estimate the damage characteristics in frozen soil under impact loading. Additionally, Sun Qiao [19] employed the fractal dimension to quantify the fragmentation morphology of sandstone subjected to freeze–thaw cycles and correlated the fractal characteristics with the initial damage and mechanical properties. Ouyang [20] focused on the quantitative description of the degree of material fragmentation based on the average particle size and fragmentation probability. Consequently, conclusions derived from freeze–thaw damage studies of concrete and rock have limited applicability and insufficient rigor when directly used to interpret the dynamic characteristics and damage evolution of cement-improved aeolian sand. In addition, although dynamic strength has been a major research focus, the effects of the cement content and freeze–thaw cycles on the multiscale dynamic mechanical properties of cement-improved aeolian sand remain unclear. Therefore, it is particularly important to investigate the freeze–thaw damage characteristics of cement-improved aeolian sand from multiple perspectives and to quantitatively elucidate the evolution of damage variables and the underlying damage mechanisms.

To address these issues, this study employed a split Hopkinson pressure bar (SHPB) apparatus to investigate the dynamic mecshanical properties, energy evolution, and fragmentation characteristics of cement-improved aeolian sand under impact compressive loading. Scanning electron microscopy (SEM) was further used to clarify the distinct roles of pore expansion, the weakening of cementation interfaces, and crack coalescence in dynamic load-bearing capacity, energy dissipation, and fragmentation refinement. On this basis, a multiscale damage analysis framework integrating macro- and microscale observations with the coupled processes of "crack evolution–energy dissipation–fragmentation fractal characteristics" was proposed. The proposed framework deepens the understanding of the impact-induced deterioration mechanism of cement-improved aeolian sand under freeze–thaw conditions and provides a theoretical basis for material design and performance evaluation in engineering applications such as subgrades and slope protection in cold regions.

2. Material and Methods

2.1. Test Materials

The raw materials used to prepare the cement-improved aeolian sand specimens were obtained from Dengkou County, Bayannur City of China (see Figure 1). This area is located in the transitional zone between desert and plain regions, where intense aeolian activity occurs and surface materials exhibit pronounced freeze–thaw weathering characteristics due to temperature fluctuations. P·O 42.5 ordinary Portland cement produced by Baoji China Conch Cement Co., Ltd. was used as the cementitious material. The basic physical properties and chemical compositions of the raw materials are presented in Tables 1 and 2, respectively.

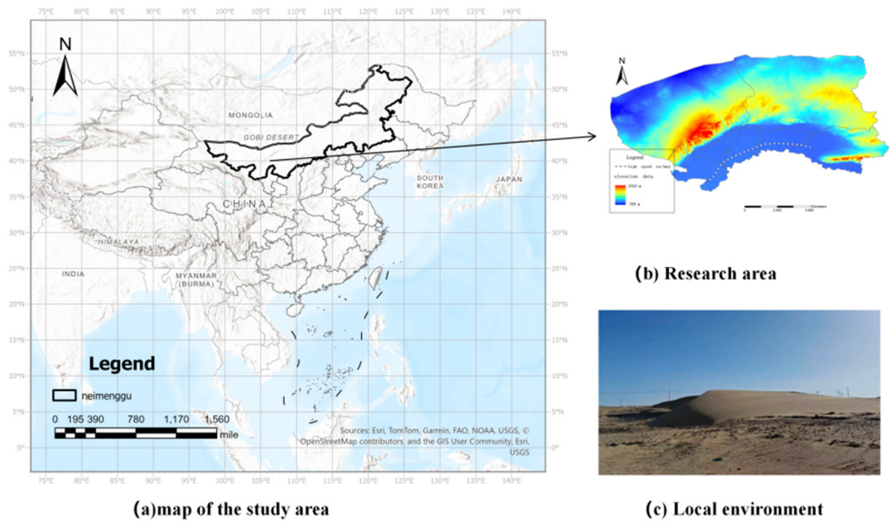

Figure 1. Map of the study area.

Table 1. Basic physical properties of aeolian sand and silt.

Name	Granular Density ($g \cdot cm^3$)	Liquid Limit (%)	Plastic Limit (%)	Dry Density ($g \cdot cm^3$)
Silt	2.67	22.6	15.3	1.71
Aeolian sand	2.65	14.8	Non-plastic	1.8

Table 2. Chemical composition of P.O42.5 retarded ordinary Portland cement.

Composition	CaO	SiO_2	Al_2O_3	MgO	Fe_2O_3	Impurity
Content (%)	61.15	22.36	7.21	4.60	4.50	0.18

The particle-size distributions are shown in Figure 2. The silt had a median particle size of d_{50} = 0.045 mm and a coefficient of uniformity of C_u = 10.08, whereas the aeolian sand had d_{50} of 0.178 mm and a C_u of 2.21. According to its particle-size characteristics, the aeolian sand was classified as uniformly graded fine sand and categorized as a Class C fill material.

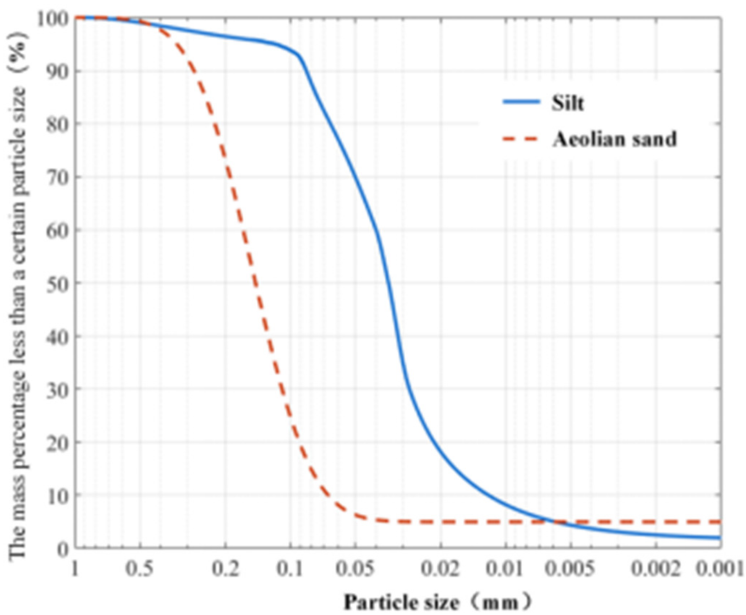

Figure 2. Particle-size distribution of aeolian sand and silt.

2.2. Test Plan

Table 3 Based on the engineering properties of cement-modified aeolian sand, a mixture with an initial cement content of 8% and a mass ratio of aeolian sand to silt of 4:6 was selected, which met the requirements for unconfined compressive strength [21]. Based on these conditions, following a 2% stepwise increment principle, three parallel groups with cement contents of 10%, 12%, and 14% were established for testing. A 4 × 4 factorial design was adopted: after 0, 5, 10, and 20 freeze–thaw cycles. Furthermore, based on the results of the preliminary impact test, using an impact pressure of 0.4 MPa and an average strain rate of 170 s^{-1} facilitates the acquisition of a sufficient number of test specimens, enabling the investigation of how cement content and the number of freeze–thaw cycles affect the impact performance of cement-modified aeolian sand.

Table 3. Test plan.

Number	Ratio of Aeolian Sand to Silt	Cement Content	Number of Freeze–Thaw Cycles
A0, A5, A10, A20	4:6	8%	0, 5, 10, 20
B0, B5, B10, B20		10%	0, 5, 10, 20
C0, C5, C10, C20		12%	0, 5, 10, 20
D0, D5, D10, D20		14%	0, 5, 10, 20

(A–D represent cement contents of 8%, 10%, 12%, and 14%, respectively, and the numbers represent the number of freeze–thaw cycles.)

2.3. Test Methods

2.3.1. Sample Preparation

According to '*The Specification for rock test of railway engineering (TB 10102-2023)*' [22] and "*Standard for Soil Testing Methods (GB/T 50123-2019)*" [23], cylindrical specimens with a diameter of 50 mm and a height of 50 mm were selected for the test. The sample preparation process is as follows: First, the material was sieved through a 5 mm round-hole sieve before being dried in an oven for 24 h to remove moisture. Subsequently, the silt, cement, and aeolian sand were mixed uniformly in the specified proportions and filled into the mold in three layers, with a compaction rate of no less than 95%. After demolding, the specimens were wrapped in plastic film and transferred to a SHBY-40B standard constant temperature and humidity curing chamber, where they were cured for 28 days at a temperature of 20 °C and a relative humidity of 95%. After curing, all specimens were immersed in distilled water at 22 °C for 24 h before freeze–thaw treatment to provide a consistent initial moisture condition. Figure 3 illustrates the specimen preparation process.

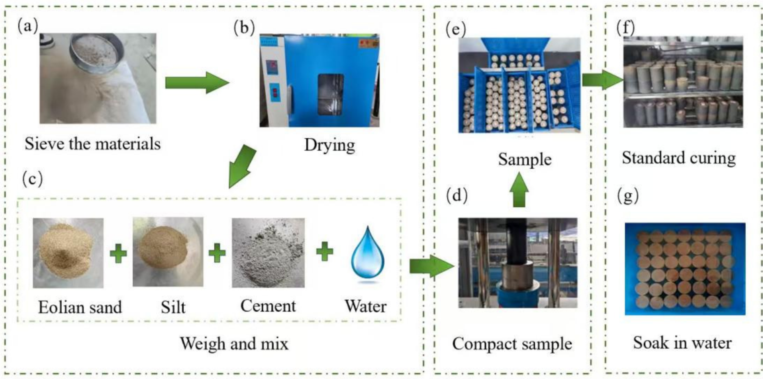

Figure 3. Sample preparation process.

2.3.2. Freeze–Thaw Cycle Test

To simulate actual freeze–thaw conditions in Inner Mongolia, the freeze–thaw cycle parameters for this test were designed in accordance with <Standard Test Methods for Long-Term and Durability Properties of Ordinary Concrete (GB/T 50082—2009)> [24]: the freezing temperature was set at −20 °C and the thawing temperature at 20 °C. The cured specimens were placed in a CC3300 low-temperature cold bath test chamber to undergo freeze–thaw cycles. Each freeze–thaw cycle lasted 10 h, including 5 h of freezing and 5 h of thawing. Figure 4 shows the temperature–time curve for the freeze–thaw cycle. The process was repeated 5, 10, and 20 times [25], resulting in modified aeolian sand specimens with varying number of cycles.

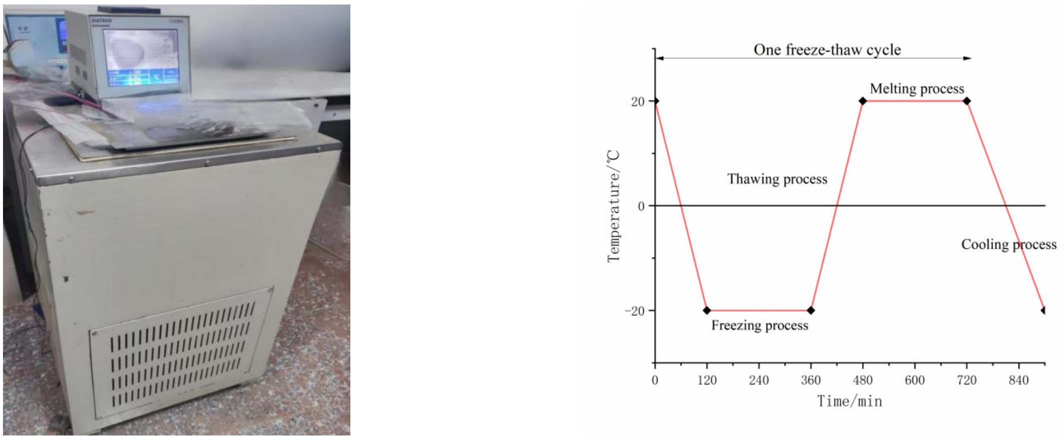

Figure 4. Temperature-time curve of freeze–thaw cycles.

2.3.3. SHPB Test

Using a split Hopkinson pressure bar apparatus, impact compression tests were performed on specimens following freeze–thaw cycles. As shown in Figure 5, the system primarily consists of a pneumatic launch mechanism, a laser velocimeter system, a super-dynamic strain acquisition subsystem, and an impact load application subsystem. The SHPB system consisted of a striker rod, an incident/rod, and a transmitted rod, with lengths of 500, 2500, and 2000 mm, respectively. All three rods had a uniform diameter of 50 mm and were manufactured from high-strength stainless steel. The bars had an elastic modulus of E = 210 GPa and sound velocity of C_0 = 5124 m/s.

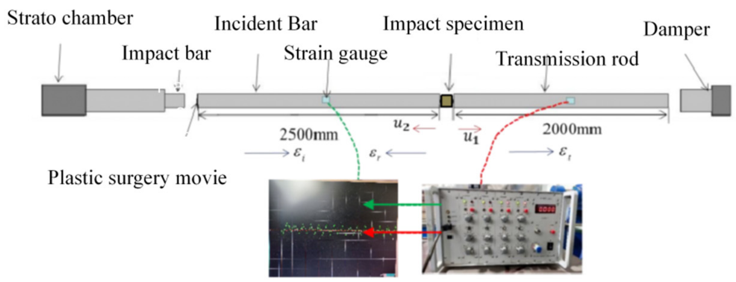

Figure 5. Hopkinson bar system.

If the forces applied to the two ends of the specimen differ in magnitude during the test, an imbalanced loading condition will result. Figure 6 depicts the stress equilibrium curve during impact loading. During impact loading, once dynamic force equilibrium is established among the incident bar, the specimen, and the transmitted bar, the stress distribution within the specimen can be considered to satisfy the one-dimensional stress-wave propagation condition. According to the split SHPB theory proposed by Kolsky, and based on the assumption of one-dimensional stress-wave propagation, the dynamic stress σ(t), strain ε(t), and strain rate $\dot{\varepsilon}_s(t)$ of the specimen can be expressed as follows:

$$\varepsilon(t) = -\frac{C_0}{L}\int_0^t [\varepsilon_i(t) - \varepsilon_r(t) - \varepsilon_t(t)]d_t \quad (1)$$

$$\sigma(t) = -\frac{A_0 E}{2A_s}[\varepsilon_i(t) + \varepsilon_r(t) + \varepsilon_t(t)] \quad (2)$$

$$\dot{\varepsilon}_s(t) = \frac{C_0}{L}[\varepsilon_i(t) - \varepsilon_r(t) - \varepsilon_t(t)] \quad (3)$$

In the equation, C_0 is the wave velocity in the member, m/s; E is the elastic modulus of the member, GPa; A_s and A_0 are the cross-sectional areas of the specimen and the member, respectively, m^2; L is the length of the specimen, m; t is time, s; and ε_i, ε_r, and ε_t denote the incident, reflected, and transmitted strain signals in the pressure bars, respectively.

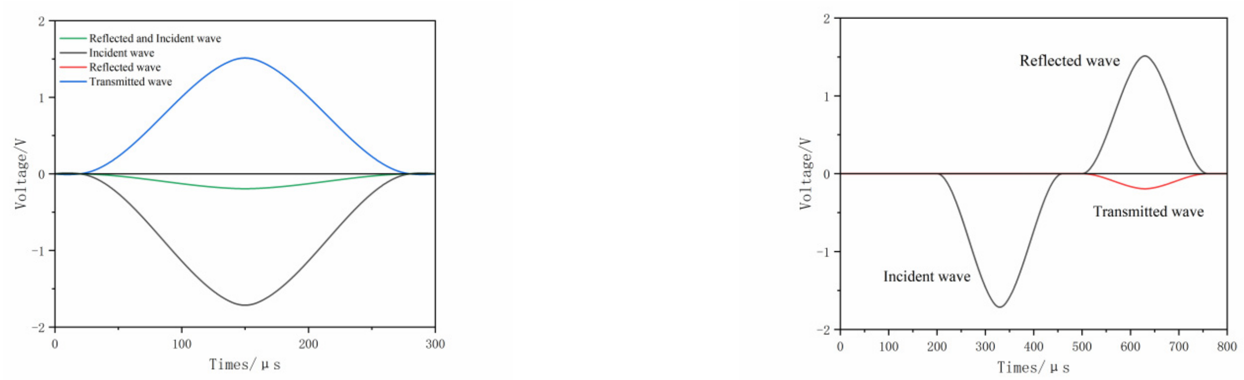

Figure 6. Schematic diagram of stress equilibrium.

3. Test Results

3.1. Stress–Strain Curve

The stress–strain curve is a significant sign for describing how mechanical properties vary throughout material failure processes. Under different freeze–thaw cycles, the stress–strain curves of specimens show similar tendencies, which can be broadly classified into four stages—the elastic expansion phase, strength enhancement phase, peak stress point, and brittle fracture phase—culminating in full fragmentation. Phase I is the elastic growth phase, in which stress rises linearly with strain while the material stays in an elastic deformation state with little internal structural changes. Phase II marks the strength enhancement phase, characterized by accelerated stress growth rates resulting from pore compression, micro-crack closure, and localized stress concentration within the specimen. The peak stress point is a key junction on the curve where fracture propagation approaches critical levels, indicating unstable failure. After reaching the maximal load-bearing capacity, specimens enter Stage III, brittle fracture, in which internal micro-cracks quickly spread and finally combine into primary cracks, resulting in structural collapse.

Figure 7 illustrates the effects of different cement levels and freeze–thaw cycles on stress–strain curves, using the 8% cement as an example. As freeze–thaw cycles increase or the cement content decreases, the slope of the elastic development phase reduces proportionally. Freeze–thaw cycles accelerate pore and micro-crack development, causing initial damage-induced voids and micro-cracks to compact more rapidly under loading, thereby entering the strength enhancement phase earlier. Concurrently, the peak stress point shifts rightward with increased freeze–thaw cycles or reduced cement content, indicating weakening elasticity and higher ductility [26]. Additionally, peak stress also shows a positive correlation with the cement content because of the formation of a gel-like product from hydration reactions, which increases the compressive strength, and a negative correlation with freeze–thaw cycles, indicating significant freeze–thaw weakening effects that lower the specimen load-bearing capacity. In contrast to low-cement formulations, the post-peak curve with a 14% cement content shows a sharp drop during the brittle fracture stages. The post-peak phases are mostly unaffected by freeze–thaw cycles.

Figure 7a shows stress–strain curves at different freeze–thaw cycles with an 8% cement content, and Figure 7b displays stress–strain curves at different cement contents without freeze–thaw cycles.

The results of the Hopkinson SHPB test are shown in Table 4.

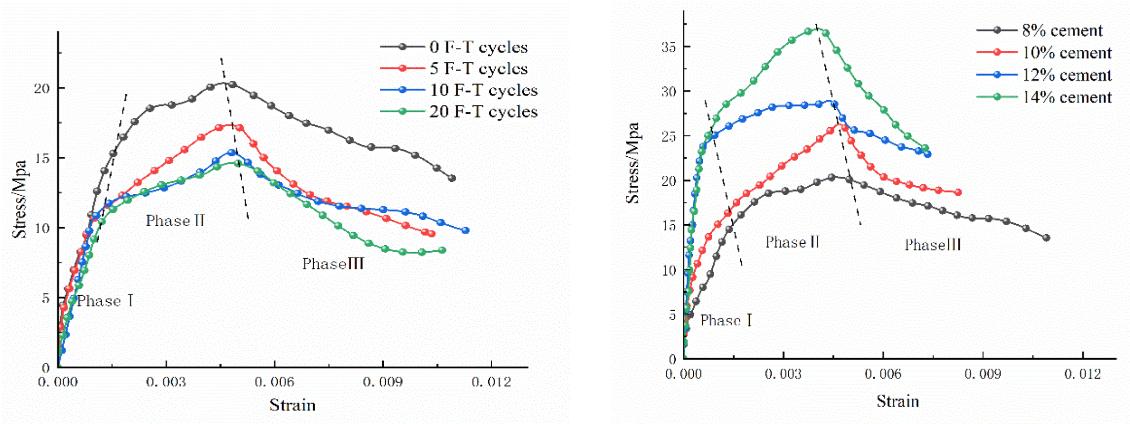

(**a**) (**b**)

Figure 7. Stress–strain curves. (**a**) shows stress–strain curves at different freeze–thaw cycles with an 8% cement content; (**b**) displays stress–strain curves at different cement contents without freeze–thaw cycles.

Table 4. SHPB test results.

Cement Content	Number of Freeze–Thaw Cycles	Peak Stress (MPa)	Peak Strain10^{-3} (%)	Energy Dissipation Density (J·cm^{-3})
8%	0	20.54	4.64	0.26197
	5	17.62	4.75	0.23325
	10	15.67	4.81	0.21597
	20	14.69	4.97	0.20203
10%	0	26.9	4.58	0.2834
	5	23.98	4.68	0.26669
	10	21.54	4.74	0.25156
	20	20.27	4.87	0.241
12%	0	29	4.42	0.29122
	5	25.9	4.55	0.27563
	10	23	4.6	0.25883
	20	21.5	4.75	0.24805
14%	0	37.09	4.06	0.4
	5	34.72	4.18	0.39312
	10	32.27	4.25	0.37768
	20	31.29	4.38	0.35805

3.2. Peak Stress

Peak stress σ_P quantifies the maximum load-bearing capacity of concrete during loading processes. Figure 8 shows the dynamic compressive strength change patterns of cement-modified aeolian sand specimens after various freeze–thaw cycles. After 0, 5, 10, and 20 freeze–thaw cycles, the dynamic compressive strengths of the specimens with an 8% cement content were 20.54, 17.62, 15.67, and 14.69 MPa, respectively. Compared with the unfrozen specimens, the corresponding reductions in dynamic compressive strength after 5, 10, and 20 freeze–thaw cycles were 14.2%, 23.7%, and 28.4%, respectively. These results indicate that the dynamic compressive strength decreased progressively with increasing numbers of freeze–thaw cycles, while the rate of strength deterioration became less pronounced after more than 10 cycles.

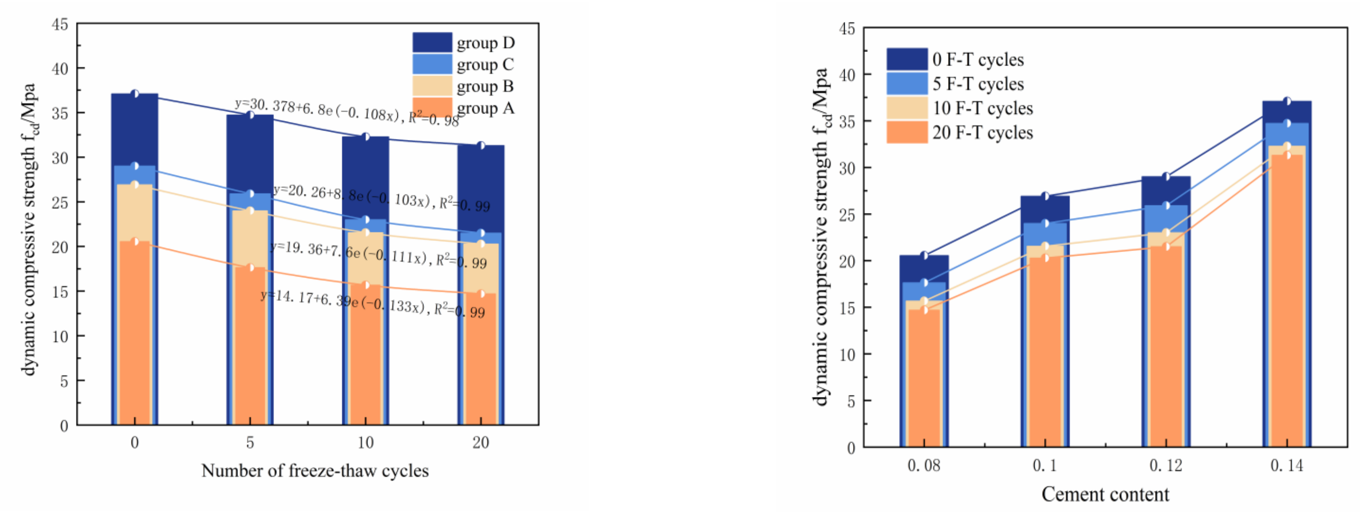

Figure 8. Characteristics of dynamic compressive strength variation.

Under the same freeze–thaw condition, the dynamic compressive strength of the cement-improved aeolian sand increased with increasing cement content. In particular, after 20 freeze–thaw cycles, the dynamic compressive strength decreased by 28.4% at a cement content of 8%, whereas the reduction was only 15.6% at a cement content of 14%. Moreover, under identical freeze–thaw conditions, specimens with lower cement contents consistently exhibited lower peak stresses than those with higher cement contents, and this difference became particularly evident at the highest cement content of 14%. These results demonstrate that increasing the cement content effectively mitigates the deterioration in dynamic compressive strength induced by freeze–thaw cycling and enhances the freeze–thaw resistance of the cement-improved aeolian sand.

3.3. Peak Strain

When rock materials are subjected to impact loads, the strain corresponding to the peak stress is referred to as dynamic peak strain ε_P. A higher peak strain indicates a better deformation capacity of the material. As shown in Figure 9, under identical cement content conditions, the peak strain exhibits a positive correlation with freeze–thaw cycles. Taking the specimens with an 8% cement content as an example, the peak strains after 5, 10, and 20 freeze–thaw cycles increased by 1.1×10^{-4}, 1.7×10^{-4}, and 3.3×10^{-4}, respectively, relative to those of the unfrozen specimens. The corresponding increases were 2.37%, 3.6%, and 7.11%, respectively. These results indicate that freeze–thaw cycling slightly enhances their deformation capacity under impact loading. Nevertheless, the overall variation in dynamic peak strain remained relatively small, suggesting that freeze–thaw cycling had a limited effect on the peak deformation characteristics. With an increasing cement content, the peak strain generally decreased. For the specimens without freeze–thaw treatment, increasing the cement content from 8% to 14% reduced the peak strain by 5.8×10^{-4}. This reduction indicates that a higher cement content enhances the resistance of cement-improved aeolian sand to deformation, resulting in a more pronounced brittle response. However, compared with its effect on dynamic compressive strength, the influence of the cement content on the peak strain was relatively limited.

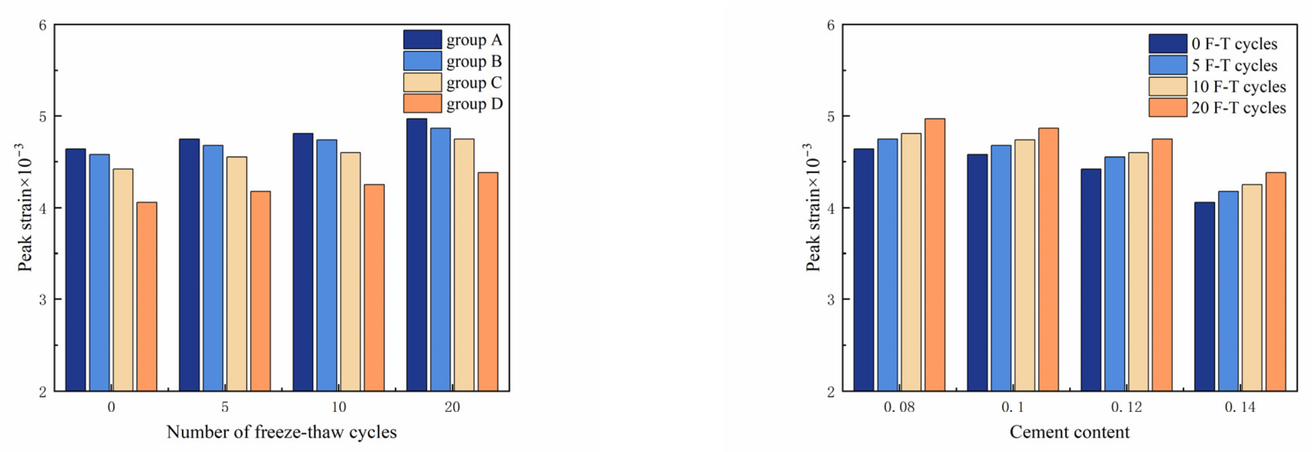

Figure 9. Characteristics of peak strain variation.

3.4. Energy Density

The damage process of specimens essentially constitutes an energy conversion process [27], where the stress states, energy levels, and specimen structure exhibit close interdependencies. Upon absorbing the energy transmitted by the SHPB device, specimens progressively accumulate internal energy until reaching their energy storage capacity threshold, resulting in structural failure. The incident energy W_I generated by bullet impact on the impact rod is partially reflected as W_R, absorbed by the specimen and dissipated through crack initiation, crack propagation, and fragment formation, and the remainder transmitted as W_T to the transmission rod. To reduce mistakes caused by specimen size fluctuations, the energy dissipation density (ω_s) is presented to quantify the energy absorption per unit volume of cement-improved aeolian sand specimens under impact loading [28].

$$W_i(t) = AEC_0 \int_0^t {\varepsilon_i}^2(t)d(t) \quad (4)$$

$$W_r(t) = AEC_0 \int_0^t {\varepsilon_r}^2(t)d(t) \quad (5)$$

$$W_t(t) = AEC_0 \int_0^t {\varepsilon_t}^2(t)d(t) \quad (6)$$

$$\omega_s = \frac{W_i - W_r - W_t}{V_s} \quad (7)$$

The formula defines $\varepsilon_i(t)$, $\varepsilon_r(t)$, and $\varepsilon_t(t)$ as the incident, reflected, and transmitted pulses on the compression rod at time t. C_0 specifies the compression rod's longitudinal wave velocity (m/s). V_s denotes the specimen volume (cm^3). The terms W_i, W_r, and W_t refer to incident, reflected, and transmitted energy. The integration interval covers the period of effective loading, where t is the end time of the effective loading pulse.

As shown in Figure 10, the energy dissipation density of cement-modified aeolian sand under dynamic loading decreases with the number of freeze–thaw cycles. The rate of reduction is rapid at the start of freeze–thaw cycles; after 10 cycles, it reduces to 10.9%, 17.5%, and 22.8%, which is consistent with the prior research findings. Freeze–thaw action causes existing micro-pores to grow or connect, lowering the material's effective bearing area and making it more vulnerable to stress concentration and speeding collapse. Increasing the cement content raises the energy dissipation density of cement-modified aeolian sand. The cement hydration products formed by the addition of cement create a continuous, robust three-dimensional spatial bonding network. Cracks cannot readily spread in a straight line through this strong cementitious network. The addition of cement increased the energy dissipation density by 0.0235, 0.0292, and 0.1894 J·cm^{-3}. As a result, the energy dissipation density of cement-modified aeolian sand increases with the cement content while decreasing with freeze–thaw cycles.

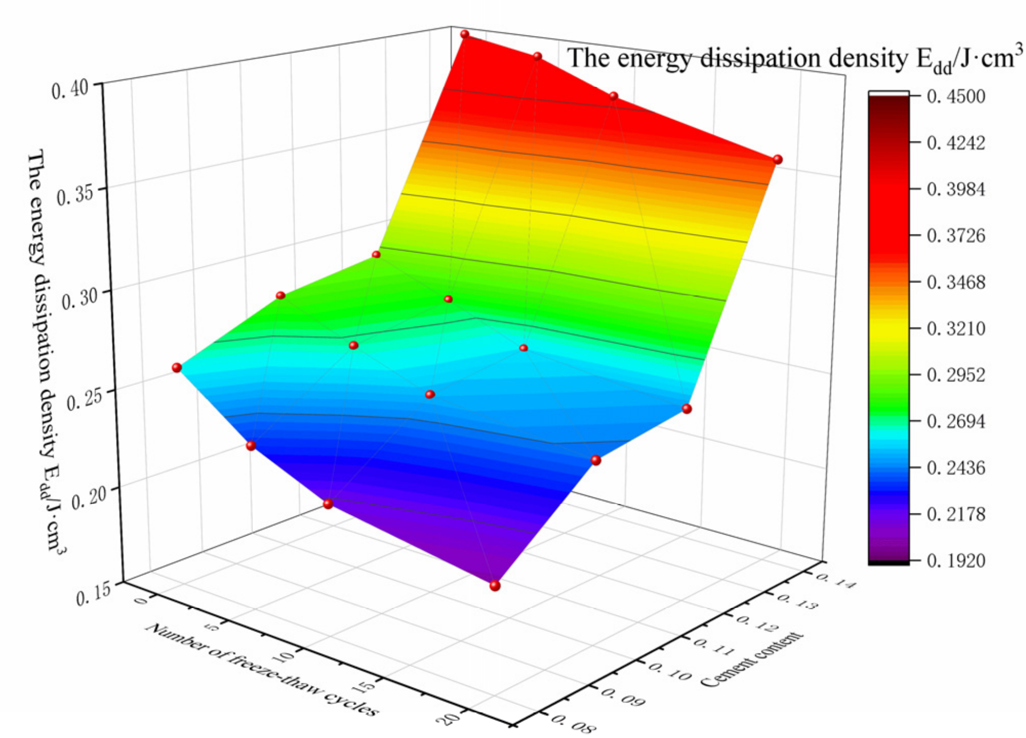

Figure 10. Energy dissipation density.

4. Fractal Properties of Fragmentation

4.1. Patterns of Fragmentation Morphology Changes

To investigate the fragmentation characteristics of modified soil under impact compression loading, the fractured fragments were collected and sieved one by one after the loading process.

Figure 11 depicts the failure patterns of cement-improved aeolian sand specimens subjected to freeze–thaw cycling containing varying cement contents. As the number of freeze–thaw cycles grows, the proportion of fine particles in the samples rises, while the uniformity of the fragmented particles decreases. After five freeze–thaw cycles, there is a noticeable increase in the proportion of fine particles in the samples. When the number of freeze–thaw cycles approaches 20, the fraction of tiny particles in the samples increases even more; compared to 10 freeze–thaw cycles, the fragmentation morphology shows a trend toward rather extreme particle sizes. Increasing the cement content minimizes fragmentation in the specimens, resulting in a more uniform and relatively concentrated particle distribution. At a 14% cement content, the specimens include big triangular prismatic shards with an irregular particle size distribution. This is because lower cement contents do not offer adequate bonding strength, making the specimens more prone to particle separation under impact, resulting in an unstable particle size distribution and an increased fraction of tiny particles following fragmentation. An excessively high cement content increases the overall rigidity of the specimens, causing the fracture mode to tend toward brittle failure, resulting in the retention of larger fragments.

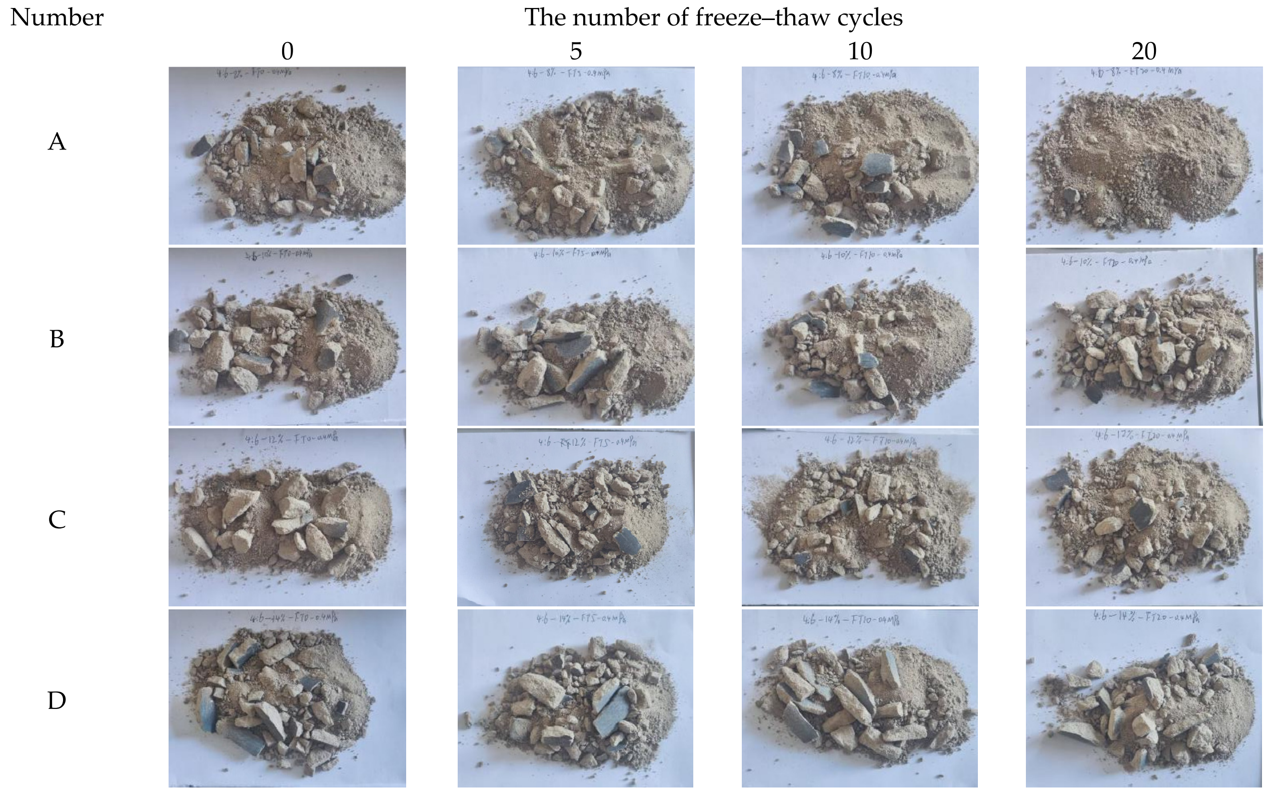

Figure 11. Sample fracture morphology.

After the impact tests, the fragmented specimens were collected and oven-dried. An 8411 electric vibrating sieve shaker was then used to separate the fragments using sieves with aperture sizes of <0.2 mm, 0.2, 0.45, 0.9, 2, 4, and 8 mm. The mass fraction of fragments retained within each particle-size range under different test conditions was calculated relative to the total fragment mass, and the results are presented in Table 5.

Table 5. Mass percentage of fragments in each size fraction after sieving.

Cement Content	Freeze–Thaw Cycles Number of Cycles	Sieve Aperture Diameter (mm) <0.2	0.2	0.45	0.9	2.0	4.0	8.0
		Mass Fraction of Fragments in Each Size Range (%)						
8%	0	11.91%	13.99%	5.00%	7.20%	4.56%	7.78%	49.55%
	5	13.76%	21.18%	9.59%	12.62%	6.22%	10.49%	26.14%
	10	18.13%	24.80%	11.04%	13.52%	7.90%	10.36%	14.24%
	20	22.61%	31.44%	12.75%	15.00%	6.15%	9.05%	2.99%
10%	0	11.23%	14.99%	6.52%	8.94%	5.24%	6.19%	46.88%
	5	11.78%	15.88%	6.82%	9.19%	5.81%	8.41%	42.11%
	10	13.54%	18.59%	5.96%	6.15%	3.37%	5.50%	46.88%
	20	16.91%	23.84%	7.76%	9.39%	5.13%	13.49%	23.47%
12%	0	9.77%	15.61%	5.32%	5.83%	3.99%	5.03%	54.45%
	5	12.04%	16.79%	7.89%	10.79%	5.94%	9.72%	36.84%
	10	13.28%	21.51%	9.48%	12.71%	6.39%	11.14%	25.49%
	20	16.87%	22.76%	10.98%	12.81%	5.59%	10.83%	20.15%
14%	0	8.73%	13.22%	6.01%	9.10%	7.12%	11.06%	44.75%
	5	11.31%	14.15%	6.22%	9.02%	6.90%	11.80%	40.60%
	10	11.67%	14.86%	6.02%	7.08%	4.55%	6.03%	50.19%
	20	12.64%	17.58%	7.00%	8.19%	4.30%	8.26%	42.03%

The particle-size distribution was consistent with the observed fragmentation morphology. With increasing numbers of freeze–thaw cycles, the proportion of fragments smaller than 0.2 mm increased, indicating a more pronounced pulverization tendency. In contrast, with an increasing cement content, the fragment-size distribution shifted toward coarser particles, with a greater proportion of fragments concentrated above 8.0 mm. This result suggests that increasing the cement content effectively suppresses fragmentation refinement and improves the integrity of cement-improved aeolian sand under impact loading.

4.2. Variation Pattern of Fractal Dimension

The fractal dimension provides a more intuitive quantitative characterization of the fragmentation characteristics of the specimens. Based on the Weibull statistical fractal theory proposed by Mandelbrot et al., the relationship between the cumulative mass and equivalent particle size of the specimen fragments can be expressed as follows [29]:

$$\left(\frac{d}{d_{\max}}\right) = \left(\frac{M_d}{M_T}\right)^{(3-D)} \tag{8}$$

Taking the base-10 logarithm of both sides of Equation (8) yields the following:

$$(3-D)\lg\left(\frac{d}{d_{\max}}\right) = \lg\left(\frac{M_d}{M_T}\right) \tag{9}$$

d represents the fragment diameter; dmax denotes the maximum diameter in the sample; M_d indicates the cumulative mass of fragments with dimensions smaller than diameter d; M_T signifies the total mass of sample fragments; D is the fractal dimension of the fragment size distribution, which quantitatively characterizes the fragmentation degree of the specimen after impact loading. A larger value of D indicates more sufficient fragmentation. This formula has been cited as Ref. [29] in the manuscript.

Accordingly, in the $\lg(M_d/M_T)$-$\lg(d/d_{max})$ coordinate system, a linear relationship can be obtained, with the slope K expressed as K = 3 − D. Therefore, the fractal dimension of the fragmented specimens can be determined using the mass–size method as D = 3 – K.

Figure 12 illustrates the relationship between the fractal dimension of specimen fragmentation and influencing factors. The progression of damage causes specimen failure and the fragment morphology. A rise in the fractal dimension implies the appearance of finer-grained particles and a decrease in the volume of larger fragments. As the number of freeze–thaw cycles increases, internal voids gradually expand into cracks and propagate outward, leading to the gradual accumulation of internal damage. The propagation of existing cracks, as well as the start and growth of new cracks, weaken the material's performance, leading to increased fragmentation and a rise in the fractal dimension, while further refining the particle size distribution. The cement percentage of 8% resulted in the most complete fragmentation and the largest fractal dimension. As the cement content increased, the fractal dimension decreased. When the cement content reached 14%, the fragmentation pattern tended toward uniformity, and the proportion of fine particles decreased slightly. The addition of cement increases the energy density required to raise the specimen's density and strengthens the material. However, the size distribution of the fragments becomes more concentrated, leading to a decrease in the fractal dimension. The fragmentation patterns upon failure are consistent with the mechanical properties.

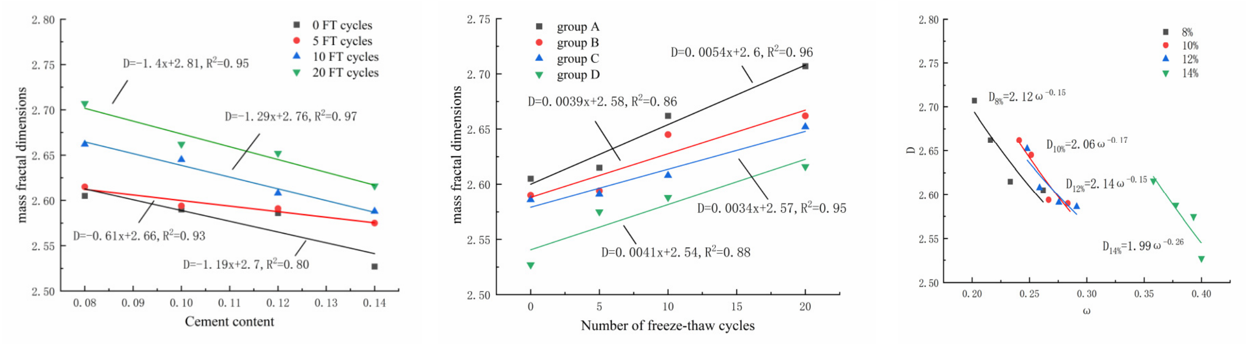

(**a**) (**b**) (**c**)

Figure 12. Effects of various variables on fractal dimension. (**a**) shows the relationship between the cement content and the fractal dimension; (**b**) shows the relationship between freeze–thaw cycles and the fractal dimension; (**c**) shows the relationship between the energy dissipation density and the fractal dimension).

Under the same test conditions, the fragmentation fractal dimension D exhibited a decreasing trend with increasing energy dissipation density ω. This inverse relationship indicates that the fragmentation behavior is associated with the pre-existing pore–crack structure generated by freeze–thaw damage, in addition to the formation of new fracture surfaces during impact failure. With increasing numbers of freeze–thaw cycles, the energy dissipation density decreased, whereas the fractal dimension increased. This behavior can be attributed to the initiation and propagation of internal microcracks induced by freeze–thaw cycling. The progressive development of these microcracks promotes pore interconnection and causes cracks to preferentially propagate along pre-damaged regions. A similar mechanism applies to cement-improved aeolian sand with different cement contents, in which the fragmentation behavior is also strongly influenced by pre-existing pores and microcracks. As the cement content decreased, the pore-filling effect and interparticle cementation were weakened, thereby reducing the resistance to crack initiation and propagation. Consequently, the specimens absorbed less impact energy prior to failure, resulting in a lower energy dissipation density. Meanwhile, the failure mode gradually changed from blocky brittle fracture to more refined fragmentation, accompanied by an increase in the proportion of fine particles and, consequently, a higher fractal dimension.

Figure 12a shows the relationship between the cement content and the fractal dimension, Figure 12b shows the relationship between freeze–thaw cycles and the fractal dimension, and Figure 12c shows the relationship between the energy dissipation density and the fractal dimension.

5. Degradation Mechanism

Figure 13 Before freeze–thaw cycles, the particles within the specimen are densely packed, and the cement hydration products are equally distributed. As the number of freeze–thaw cycles increases, the pore structure expands and cracks form and penetrate through the specimen. After twenty cycles, significant flaking of the cement hydration products is observed, with particle detachment and pore connectivity appearing in some areas, forming distinct failure paths. Cracks form rapidly as a result of freeze–thaw cycles, with micro-cracks extending from weak zones into the aggregate zone [30], resulting in a large number of cementitious and particle fractures. Therefore, the coalescence and interconnection of cracks promote fragmentation refinement and pulverization, thereby increasing the fractal dimension. Concurrently, indentations associated with the ductile fracture morphology were observed. During the fracture process, the applied energy was consumed and absorbed to form and propagate internal cracks within the specimen, leading to increased internal damage. Consequently, the specimen's ability to resist deformation progressively weakened, resulting in fracture under relatively low loads and ultimately yielding a lower overall strength and stiffness.

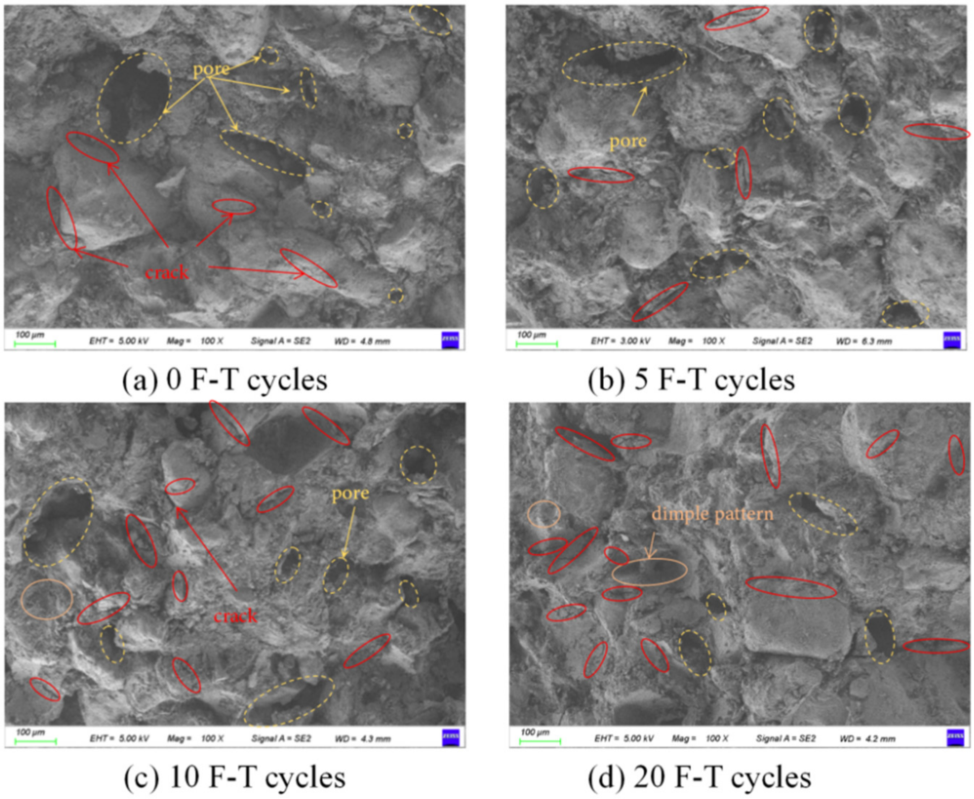

Figure 13. Microscopic morphology of Group B under different freeze–thaw cycles.

Figure 14 As the cement content grew, the cementitious layer of the specimens became more uniform, with cement hydration products completely filling the interparticle gaps, resulting in a considerable decrease in porosity. At a 12% cement content, the porosity decreased and the volume of cementitious products increased; however, a continuous matrix had not yet developed, resulting in many cracks in weak zones. Due to the reduction in internal defects, the stress concentration decreased; at the same time, improved cementation strengthened the connections between particles. This requires the material to accumulate a higher energy to trigger the crack propagation, resulting in an increased macroscopic compressive strength and energy dissipation density. Although crack propagation must overcome greater resistance after reaching peak stress, once a crack penetrates, the accumulated high elastic energy is immediately released, accelerating the material's fracture rate and displaying more pronounced brittle characteristics, such as laminar tearing and cleavage steps on the fracture surface [31,32]. The fracture route is generally regular, and the resulting fragments are larger and simpler in shape, with a lower fractal dimension. During the fracture process, the energy input from the external load is primarily consumed by brittle deformation; the modified soil exhibits a higher strength and stiffness, but its deformation capacity is somewhat reduced [15].

Simultaneously, a high cement content forms a more compact matrix, significantly reducing the material porosity. The fundamental mechanism of freeze–thaw damage stems from internal stresses generated by pore water freezing and expansion. With a reduced total pore volume and narrowed pore diameters, the amount of freezable water decreases substantially, consequently weakening the frost heave forces. As a result, even after repeated freeze–thaw cycles, materials with a high cement content exhibit a slower accumulation of internal damage, thereby maintaining superior strength retention rates.

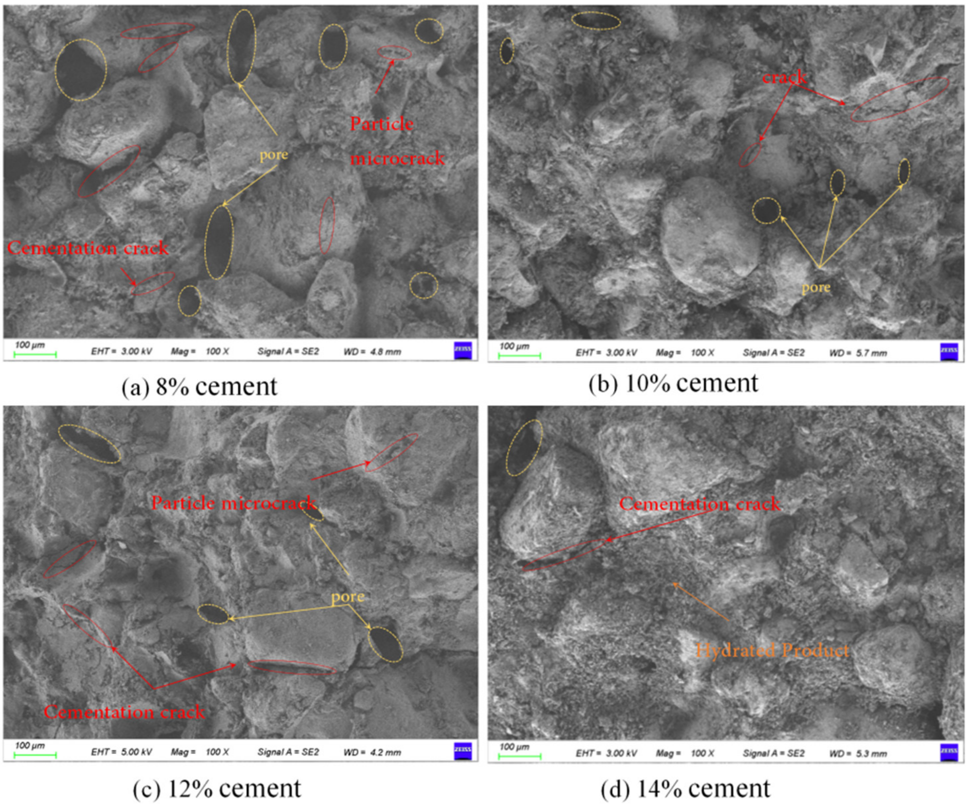

Figure 14. Microscopic morphology at different cement content levels.

SEM images were further processed using image analysis to quantitatively characterize the two-dimensional pore area fraction under different test conditions. Figure 15 presents the relationships between the SEM-derived apparent porosity and the macroscopic mechanical parameters. Strong linear correlations were observed between the apparent porosity and both the peak stress and peak strain, indicating that the evolution of the pore structure is closely associated with the degradation of the dynamic mechanical response of cement-improved aeolian sand. The correlations of the fractal dimension and energy dissipation density with apparent porosity were comparatively lower, with coefficients of determination (R^2) of approximately 0.75. These results suggest that fragmentation characteristics and energy dissipation are not controlled by porosity alone, but are also influenced by the coupled development of pores, microcracks, interparticle debonding, and cementation damage.

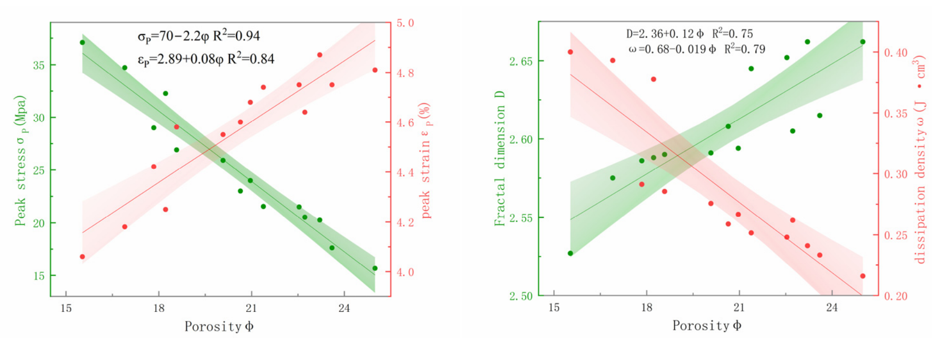

Figure 15. Linear correlations between macroscopic and microscopic parameters.

6. Discussion

6.1. Freeze–Thaw Degradation Function

The mechanical properties and macroscopic failure characteristics are directly related to freeze–thaw damage. To eliminate the influence of differences in the initial properties of specimens with different cement contents, the dynamic peak strength loss ratio $D_\sigma(N)$ and the energy dissipation density loss ratio $D_\omega(N)$ are defined as follows [33]:

$$D_\sigma(N) = 1 - \frac{\sigma_N}{\sigma_0} \tag{10}$$

$$D_\omega(N) = 1 - \frac{\omega_N}{\omega_0} \tag{11}$$

where N denotes the number of freeze–thaw cycles; σ_N and ω_N denote the dynamic peak strength and energy dissipation density after N freeze–thaw cycles, respectively; and σ_0 and ω_0 denote the corresponding values of the specimens without freeze–thaw treatment.

To investigate the relationship between the number of freeze–thaw cycles and the overall damage evolution, the Weibull probability density function was employed to characterize the freeze–thaw failure probability of material microelements, as expressed in Equation (12). Accordingly, the cumulative failure degree $D_f(N)$ after N freeze–thaw cycles can be obtained from Equation (13) [34]:

$$f(N) = \frac{\beta}{\alpha}\left(\frac{n}{\alpha}\right)^{\beta-1} \cdot \exp\left[-(\frac{N}{\alpha})^{\beta}\right] \tag{12}$$

$$D_f(N) = \int f(N)dN = 1 - \exp[-(\frac{N}{\alpha})^{\beta}] \tag{13}$$

A freeze–thaw damage tolerance parameter, λ, was further introduced to account for the material resistance to freeze–thaw deterioration. A smaller λ indicates the stronger freeze–thaw resistance of the cement-improved aeolian sand [33]. The cumulative damage degree D(N) after N freeze–thaw cycles is therefore expressed by Equation (14). By substituting Equations (10) and (11) into Equation (13), the fitting parameters were obtained, as listed in Table 6:

$$D(N) = \lambda D_f(N) = \lambda \cdot \left\{1 - \exp\left[-\left(\frac{N}{\alpha}\right)^{\beta}\right]\right\} \tag{14}$$

Table 6. Model-fitting parameters.

Cement Content	Modified Weibull Distribution Model						
	λ_σ	λ_ω	α_σ	α_ω	β_σ	β_ω	R2
8%	0.287	0.246	6.64	8.15	1.35	1.08	0.999
10%	0.245	0.151	6.80	8.2	1.20	1.35	0.992
12%	0.267	0.150	7.89	8.34	1.33	1.61	0.996
14%	0.156	0.110	7.23	11.89	1.75	2.05	0.999

According to the λ index, the freeze–thaw resistance of specimens with different cement contents did not exhibit a strictly monotonic variation with the cement content. At relatively low cement contents, the specimen with 10% cement exhibited favorable freeze–thaw resistance and a relatively strong capacity to withstand long-term freeze–thaw damage. The specimen with 12% cement showed superior resistance during the early stages of freeze–thaw cycling, which may be attributed to the formation and development of hydration products. However, under prolonged freeze–thaw exposure, the rate of damage accumulation increased. This behavior may be related to the evolution of the internal cemented structure: at a cement content of 12%, the material remained in a transitional structural state, and a fully continuous and stable cemented skeleton had not yet formed. In addition, the variation in porosity at a 12% cement content was more pronounced than that at 10%. When the cement content increased to 14%, the dominant load-bearing mechanism gradually shifted from a particle-dominated skeleton to a cementation-dominated structure. The formation of a more continuous cemented framework enhanced the structural integrity of the material and consequently improved its resistance to freeze–thaw deterioration.

The modified Weibull distribution model exhibited a high goodness of fit for cement-improved aeolian sand subjected to freeze–thaw cycling and effectively characterized the progressive damage degradation associated with increasing numbers of freeze–thaw cycles (Figure 16). With further validation, the proposed model may provide a useful basis for the optimized design and durability assessment of cement-improved aeolian sand under freeze–thaw environments. An analysis of the characteristic freeze–thaw cycle parameters showed that all four cement contents satisfied $> \alpha\sigma$, indicating that the dynamic load-bearing capacity responded to freeze–thaw damage earlier than the energy dissipation capacity exhibited pronounced degradation. This finding is consistent with the conclusion reported by Baker [35] that the peak stress provides a more sensitive indicator of material failure.

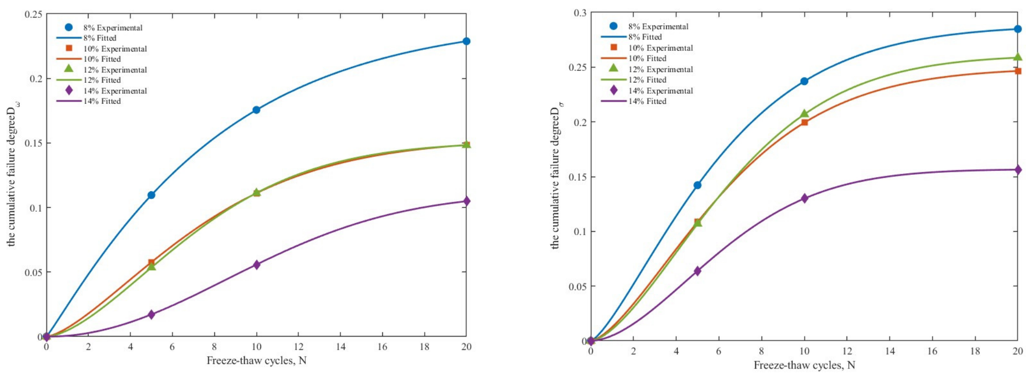

Figure 16. Prediction of freeze–thaw damage under impact loading.

6.2. Material Brittleness Analysis

Han [36] quantified material brittleness B (Equation (15)) using pre-peak and post-peak energy measurements. Rock brittleness manifests as the capacity to accumulate elastic energy before peak deformation and demonstrates a self-sustaining fracture propagation capability after peak. A smaller brittleness-index value indicates a greater tendency toward brittle failure. Figure 17 illustrates the brittleness index of modified aeolian sand versus the cement content. As the cement content increased, the brittleness index B generally decreased, indicating a progressively stronger tendency toward brittle failure. For specimens with cement contents of 8% and 10%, the B values were approximately 0.584 and 0.569, respectively, showing only a minor difference. When the cement content increased to 12%, B decreased markedly to approximately 0.463, representing a reduction of about 18.6% relative to that at a 10% cement content and indicating a pronounced increase in material brittleness. A further increase in cement content to 14% resulted in only a marginal change, with B remaining at approximately 0.462.

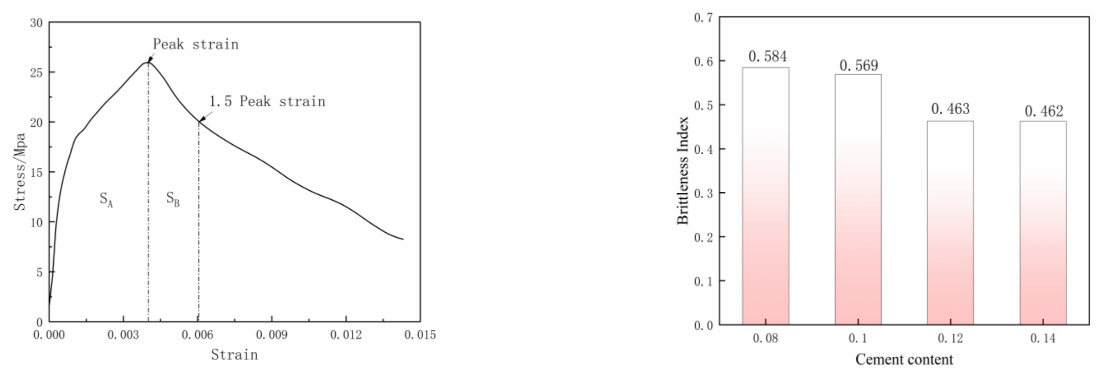

Figure 17. Brittle index.

Therefore, the cement-content range of 10–12% can be regarded as a critical transition interval from relatively ductile failure to highly brittle failure. Beyond a 12% cement content, the additional improvements in strength and freeze–thaw resistance should be evaluated in conjunction with the associated increase in brittleness risk.

$$B = \frac{S_a}{S_b} \tag{15}$$

where S_b represents the energy absorbed or released after the peak, and S_a represents the energy absorbed or released before the peak.

6.3. Engineering Applications

To reveal the similarities in the material strength and engineering applicability of cement-improved aeolian sand under impact and freeze–thaw conditions, this section compares the properties of cement-improved aeolian sand with those of other common similar materials, such as sandstone [37] and basalt fiber concrete [38] (under the same experimental conditions). A comparison was conducted based on the peak strain, peak stress, energy dissipation density, freeze–thaw resistance, and brittleness indices. Meanwhile, this study analyzes the construction costs associated with concrete production and the carbon costs incurred during transportation as green economic indicators (Table 7). All indicators are dimensionless values. These dimensionless values were calculated using basalt fiber concrete as the standard, obtained by dividing the test values of each material group by the standard value.

As shown in Figure 18, under the same impact conditions, the dynamic strength of cement-modified aeolian sand is comparable to that of basalt fiber concrete, demonstrating a good load-bearing capacity. After freeze–thaw cycles, the deterioration trend of cement-modified aeolian sand is relatively mild, with an overall decline similar to that of sandstone. In summary, cement-modified aeolian sand not only maintains a good level of strength under freeze–thaw conditions, but also exhibits a freeze–thaw resistance comparable to various natural rock types at a 14% cement content. It is suitable for engineering environments in cold regions or those subject to frequent freeze–thaw cycles. Within the investigated range, a cement content of approximately 10% provided a favorable balance among the dynamic strength, freeze–thaw durability, deformation capacity, and cement consumption. It is therefore recommended as a reference cement content for railway subgrades and fill engineering in cold regions. For slope protection or localized reinforcement subjected to more severe freeze–thaw environments, a higher cement content may be adopted when a greater residual strength and durability are required. However, when the cement content reaches 12% or higher, the associated increases in stiffness and brittleness should be carefully considered, as rapid crack propagation and localized brittle failure may become more pronounced.

Table 7. Green economy indicators.

Material	Carbon Emission (kg CO_2e/kg)	Carbon Cost (RMB/kg)	Direct Cost (RMB/kg)	Comprehensive Cost (RMB/kg)	Dimensionless Scaling of Indicators
8% cement-improved soil	0.0581	0.0052	0.0617	0.0669	2.51
10% cement-improved soil	0.0699	0.0063	0.0682	0.0745	2.26
14% cement-improved soil	0.0936	0.0084	0.0805	0.0889	1.89
Basalt-fiber-reinforced concrete	0.25	0.0225	0.146	0.1685	1

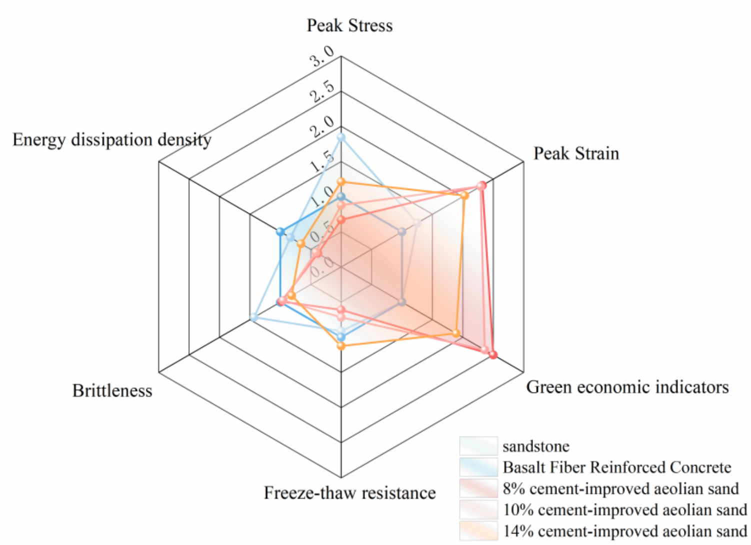

Figure 18. Comparison of material properties.

This study provides experimental evidence for the damage evolution and dynamic failure mechanisms of cement-improved aeolian sand under freeze–thaw conditions, and it proposes an engineering-oriented mix-design framework that takes into account the load-bearing capacity, freeze–thaw durability, deformation characteristics, brittleness, and cement consumption. The findings provide an experimental foundation for the material selection and durability testing of cement-improved aeolian sand utilized in subgrades, slopes, and protective structures in cold climates. Future research should use high-speed imaging and other in situ monitoring techniques to investigate material behavior and crack evolution under long-term freeze–thaw cycling and multiple strain-rate conditions, which will improve the accuracy of engineering performance prediction and durability design.

7. Conclusions

This study investigated the dynamic behavior and deterioration mechanisms of cement-improved aeolian sand subjected to freeze–thaw cycling using SHPB impact tests, fragmentation analysis, and SEM observations. The main conclusions are as follows:

(1) With increasing freeze–thaw cycles, the dynamic compressive strength and energy dissipation density decreased exponentially, whereas the peak strain increased slightly. The deterioration rate slowed markedly after 10 cycles. Increasing the cement content improved the freeze–thaw resistance; after 20 cycles, the strength loss decreased from 28.4% at a 8% cement content to 15.6% at 14%. A modified Weibull model incorporating the freeze–thaw damage tolerance parameter effectively described the degradation of dynamic mechanical properties.
(2) An increasing freeze–thaw damage or decreasing cement content reduced the energy dissipation density and increased the fractal dimension, accompanied by a transition from blocky fracture to refined fragmentation and pulverization. A clear power-law relationship was observed between the energy dissipation density and fractal dimension, indicating a strong coupling between energy dissipation and fragmentation evolution.
(3) SEM observations showed that freeze–thaw cycling promoted pore expansion and crack coalescence, whereas an increasing cement content mitigated these effects through pore filling and enhanced cementation. At a 14% cement content, the excessive accumulation of hydration products increased the brittleness and resulted in more pronounced lamellar fracture characteristics.

In conclusion, this study clarified the dynamic degradation characteristics of cement-improved aeolian sand and established a freeze–thaw damage evolution model. By linking laboratory-scale observations with potential engineering behavior, a multiscale analytical framework for the freeze–thaw–impact deterioration of cement-improved aeolian sand was developed, integrating the dynamic mechanical response, energy dissipation, fragmentation evolution, and microstructural damage. The findings provide a theoretical basis for material design and performance evaluation in subgrade and slope-protection engineering in cold regions.

Author Contributions: Conceptualization, and methodology, X.L.; formal analysis, K.R., X.L., and Y.Q.; resources, K.R.; writing—original draft preparation, K.R. and X.P.; writing—review and editing, K.R. and X.L., project administration, X.L. All authors have read and agreed to the published version of the manuscript.

Funding: This research was funded by the Major Projects Programme of China Railway Beijing Engineering Group Co., Ltd. (Project No.: 2023A-Major Projects-005) and the Key Research and Development Project under the Weinan Municipal Science and Technology Programme (25ZDYFJH-983).

Data Availability Statement: The data are contained within the article.

Acknowledgments: Thank you to all the authors for their dedication to completing the paper. We would like to thank all the authors for their efforts in completing this paper.

Conflicts of Interest: Authors Xun chang Li Ke xin Ren and Yuang Qiare are employed by Chang'an University. Author Xun chang Li is employed by the Ministry of Education Key Laboratory of Mineral Resources and Geological Engineering in Western China. Author Xuqing Pang is employed by Shaanxi Railway Vocational and Technical College. This study was conducted without any commercial or financial relationships that could be considered a potential conflict of interest.

References

1. Du, W.; Nie, R.; Qi, Y.; Ruan, B.; Mo, F. Investigation on the static performance of geogrid reinforced aeolian sand railway embankment: Field test and discrete element simulation. *Geotext. Geomembr.* **2024**, *52*, 736–752. [CrossRef]
2. Li, G.; Zhu, Q.; Liu, J.; Wang, P.; Liu, X. Shear Strength Characteristics of Aeolian Sand Solidified by Microbially Induced Calcite Precipitation (MICP). *Soil Mech. Found. Eng.* **2025**, *62*, 363–370. [CrossRef]
3. He, R.; Han, D.; Li, L.; Li, R.; Hu, Y. Application Review of Aeolian Sand Used in Road Engineering. *Chin. J. Highw. Transp.* **2025**, *38*, 1–30. [CrossRef]

4. Liu, J.; Liu, Q.; Liu, X.; Li, K.; Hu, C.; Ai, Y. Spatial dynamic response of aeolian sand subgrade reinforced by geocell. *Water Resour. Hydropower Eng.* **2026**, *57*, 187–201. Available online: https://link.cnki.net/urlid/10.1746.TV.20260317.1853.002 (accessed on 10 September 2026).
5. Fathi-Moghaddam, M.; Tavakol-Sadrabadi, M.; Tajbakhsh, M. Effect of Lime and Rice Husk Ash on Horizontal Saturated Hydraulic Conductivity of Sandy Loam Soils. *Geotech. Geol. Eng.* **2020**, *38*, 2027–2037. [CrossRef]
6. Bai, J.; Xu, R.; Zhao, Y.; Shi, J. Flexural fatigue behavior and damage evolution analysis of aeolian sand concrete under freeze–thaw cycle. *Int. J. Fatigue* **2023**, *171*, 107583. [CrossRef]
7. de Jesús Arrieta Baldovino, J.; dos Santos Izzo, R.L.; Rose, J.L. Effects of Freeze–thaw Cycles and Porosity/cement index on Durability, Strength and Capillary Rise of a Stabilized Silty Soil Under Optimal Compaction Conditions. *Geotech. Geol. Eng.* **2021**, *39*, 481–498. [CrossRef]
8. Cui, B.; Xu, J.; Shao, X.; Xu, D.; Zhang, B. Static Mechanical Properties of Aeolian Sand Improved with Silt Subjected to Varying Temperature and Pressure. *Buildings* **2024**, *14*, 3801. [CrossRef]
9. Chen, R.; Chen, H.; Fan, Z.; Xu, F.; Li, J.; Wu, Y. Experimental study on the unsaturated shear strength of stabilizedaeolian sand considering geopolymer content. *J. Southeast Univ. (Nat. Sci. Ed.)* **2026**, *56*, 302–311. Available online: https://link.cnki.net/urlid/32.1178.n.20251010.1106.004 (accessed on 10 September 2026).
10. Chen, R.; Chen, H.; Hao, R.; Bao, W.; Li, L.; Luo, W. Stress-strain-strength characteristics and microstructure ofgeopolymer stabilized aeolian sand. *J. Zhejiang Univ.* **2025**, *59*, 177–186. [CrossRef]
11. Ruan, B.; Shen, Y.; Zhang, X.; Lu, Z.; Zhang, J.; Nie, R. The effects of freeze-thaw cycle on the dynamic characteristics of cemented aeolian sand reinforced with basalt fiber. *J. Railw. Sci. Eng.* **2025**, *22*, 1614–1621. [CrossRef]
12. Hao, L.; Zhou, Y.; Yuan, Z. Study on frost resistance and life prediction of hybrid fiber aeolian sand concrete. *J. Irrig. Drain. Eng.* **2025**, *43*, 275–283.
13. Wang, L.; Zhao, J. Research on pore characteristics and dynamic mechanical properties of road CFB ash concrete under the influence of seasonal freezing. *J. North China Univ. Water Resour. Electr. Power* **2024**, *45*, 92–99. [CrossRef]
14. Dong, Z.; Yang, G.; Bi, J.; Zhao, T.; Zhao, K.; Wang, H. Experimental study on the mode I fracture of hybrid fiber-reinforced cementitious composites under high loading rate. *Theor. Appl. Fract. Mech.* **2026**, *143*, 105505. [CrossRef]
15. Zhang, M.; Fan, J.; Yang, W.; Li, Z.; Chen, J.; Jiang, D.; Li, Y.; Nelias, D. Experimental study on dynamic fracture and fragmentation behavior of surrounding rock in salt cavern gas storage under impact loading. *Eng. Fract. Mech.* **2025**, *328*, 111559. [CrossRef]
16. Shu, Y.-H.; Zhang, J.-S.; Fang, A.-N.; Wu, Y.-Q.; Qin, R.-H.; Miao, P. Effect of coupled chloride salt erosion and Freeze-thaw on the dynamic mechanical properties of EPS cement soils. *Constr. Build. Mater.* **2023**, *375*, 130951. [CrossRef]
17. Luo, H.; Jiang, J.; Zhao, K. Damage characteristics of basalt fiber recycled concrete under freeze-thaw cycle based on energy dissipation. *Compos. Sci. Eng.* **2023**, *5*, 86–93. [CrossRef]
18. Zhu, Z.; Zhang, T.; Wang, Y.; Ma, Y.; Cheng, Z. Damage mechanism and energy evolution of frozen soil under coupled compression–shear impact loading. *Cold Reg. Sci. Technol.* **2025**, *230*, 104361. [CrossRef]
19. Qiao, S.; Luping, S.; Zehui, Y. Experimental study on dynamic impact characteristics of sandstone subjected to freeze-thaw cycles. *Bull. Geol. Sci. Technol.* **2026**, *45*, 171–184. [CrossRef]
20. Ouyang, H.; Gong, Z.; Qin, W. Dynamic behaviors and particle breakage evolution of calcareous sand under repeated one-dimensional impacts. *J. Vib. Shock* **2025**, *44*, 16–25+34. [CrossRef]
21. Li, X.; Miao, C.; Shi, Z. Evolution of Pore Structure and Damage Mechanism Analysis of Cement–Silt-Modified Eolian Sand Under Freeze–Thaw Cycles. *Materials* **2025**, *18*, 3800. [CrossRef]
22. *TB 10102-2023*; Specification for Rock Test of Railway Engineering. China Railway Publishing House: Beijing, China, 2023.
23. *GB/T 50123-2019*; Standard for Soil Testing Methods. China Architecture & Building Press: Beijing, China, 2019.
24. *GB/T 50082—2009*; Standard Test Methods for Long-Term and Durability Properties of Ordinary Concrete. Ministry of Housing and Urban-Rural Development of PRC: Beijing, China, 2009.
25. Li, T.; Wu, P.; Hu, S.; Wu, B.; Chen, Z. Cyclic impact experimental study on the mechanical behavior of sandstone subjected to freeze-thaw cycles. *Front. Earth Sci.* **2025**, *13*, 1661900. [CrossRef]
26. Wang, X.; Li, R.; Zhou, H.; Mu, C.; Qiao, Q. Experimental investigation on discreteness of quasi-static and dynamic compressive strength of recycled aggregate concrete. *J. Compos. Mater.* **2024**, *41*, 3092–3102. [CrossRef]
27. Yang, R.; Xu, Y.; Chen, P.; Wang, J. Experimental study on dynamic mechanics and energy evolution of rubber concrete under cyclic impact loading and dynamic splitting tension. *Constr. Build. Mater.* **2020**, *262*, 120071. [CrossRef]
28. Zheng, Q.; Li, P.; Xu, Y.; Yin, Z.; Hu, H. Energy Evolution and Dynamic Response of Pre-damaged Sandstone under Impact Loading. *Eng. Sci. Technol.* **2025**, *57*, 1–14. Available online: https://link.cnki.net/urlid/51.1773.TB.20250305.0922.004 (accessed on 10 September 2026).
29. Du, W.; Zhang, D.; Yu, B. Mechanical and fractal characteristics of sandstone with Pre-existing fissures of different lengths under varying impact loads in SHPB tests. *Theor. Appl. Fract. Mech.* **2023**, *125*, 103884. [CrossRef]

30. Gai, W.; Dai, F.; He, B.; Zhou, C.; Wei, M.; Liu, Y. Influence of GGBFS and alkali activators on macro-mechanical performance and micro-fracture mechanisms of geopolymer concrete in split Hopkinson pressure bar tests. *Constr. Build. Mater.* **2024**, *434*, 136736. [CrossRef]
31. Yin, X.; Guo, Q.; Shi, Z.; Yan, J.; Guo, Y.; Li, F. Coupled effects of subzero temperature and impact loading on the dynamic mechanical properties and fracture mechanism of dolomite. *Cold Reg. Sci. Technol.* **2026**, *243*, 104774. [CrossRef]
32. Li, Z.; Yang, G.; Wang, B.; Wang, J. Study on unfrostered water content and strength characteristics of saturated sandstone during thawing process. *Sci. Rep.* **2025**, *15*, 17641. [CrossRef]
33. Wang, P.; Xu, J.; Fang, X.; Wang, P. Energy dissipation and damage evolution analyses for the dynamic compression failure process of red-sandstone after freeze-thaw cycles. *Eng. Geol.* **2017**, *221*, 104–113. [CrossRef]
34. Fang, Z.; Zou, F.; Tang, X. Study on Energy Dissipation and Damage Evolution Laws of Limestone under Impact Loading. *Chin. J. Undergr. Space Eng.* **2020**, *16*, 475–483. [CrossRef]
35. Baker, T.H.W. Strain rate effect on the compressive strength of frozen sand. *Eng. Geol.* **1979**, *13*, 223–231. [CrossRef]
36. Han, M. Evaluation of Rock Brittleness Index and Numerical Analysis of Roller Bit Rock Breaking. Ph.D. Thesis, Central South University, Changsha, China, 2023. [CrossRef]
37. Li, C. Research on the Dynamic Mechanical Behavior of Frozen-Thawed Sandstone in Saturated and Frozen States. Master's Thesis, Central South University, Changsha, China, 2023.
38. Li, X.; Xiao, D.; Pu, C.; Yue, B.; Long, Y.; Li, X.; Pei, G. Study on dynamic compression failure and energy dissipation characteristics of basalt fiber concrete under freeze-thaw. *Chem. Ind. Miner. Process.* **2024**, *53*, 24–33. [CrossRef]

https://doi.org/10.3390/buildings16183673